FULL PAPER
FUNCTIONAL MATERIALS
www.afm-journal.de
www.MaterialsViews.com

Temperature-Dependent Charge-Carrier Dynamics in $CH_3NH_3PbI_3$ Perovskite Thin Films

*Rebecca L. Milot, Giles E. Eperon, Henry J. Snaith, Michael B. Johnston, and Laura M. Herz**

The photoluminescence, transmittance, charge-carrier recombination dynamics, mobility, and diffusion length of $CH_3NH_3PbI_3$ are investigated in the temperature range from 8 to 370 K. Profound changes in the optoelectronic properties of this prototypical photovoltaic material are observed across the two structural phase transitions occurring at 160 and 310 K. Drude-like terahertz photoconductivity spectra at all temperatures above 80 K suggest that charge localization effects are absent in this range. The monomolecular charge-carrier recombination rate generally increases with rising temperature, indicating a mechanism dominated by ionized impurity mediated recombination. Deduced activation energies E_a associated with ionization are found to increase markedly from the room-temperature tetragonal ($E_a \approx 20$ meV) to the higher-temperature cubic ($E_a \approx 200$ meV) phase adopted above 310 K. Conversely, the bimolecular rate constant decreases with rising temperature as charge-carrier mobility declines, while the Auger rate constant is highly phase specific, suggesting a strong dependence on electronic band structure. The charge-carrier diffusion length gradually decreases with rising temperature from about 3 µm at –93 °C to 1.2 µm at 67 °C but remains well above the optical absorption depth in the visible spectrum. These results demonstrate that there are no fundamental obstacles to the operation of cells based on $CH_3NH_3PbI_3$ under typical field conditions.

1. Introduction

Perovskites of the form AMX_3, where A is an organic cation, M is a metal cation, and X is a halide anion, have emerged as promising new materials for photovoltaic cells.[1] Following their initial success as sensitizing layers for dye-sensitized solar cells[2] and their subsequent use as standalone thin-film active layers,[3] perovskites have quickly become one of the most promising low-cost alternatives to traditional semiconductors.[1a,b] Although efficiencies of perovskite solar cells were modest at the start, devices now regularly achieve efficiencies of ≈15%, with the current record exceeding 20% and projections for tandem devices promising 30%.[1d,4] In addition, hybrid metal halide perovskites have been shown to be promising candidates as active materials for light emission and lasing.[5]

The appeal of perovskites for use in photovoltaics lies in their unique chemical and physical properties. In addition to their relative ease of synthesis from simple starting materials through solution processing[1b,6] or vapor deposition[7] methods, they also have bandgap energies in the near-infrared (NIR) close to the Shockley–Queisser ideal and exhibit high extinction coefficients across the visible spectrum.[1a] Furthermore, band-gap energies can be easily tuned with chemical com position.[1a,e,f,8] The success of perovskites is further explained by their high charge-carrier mobilities (8–33 $cm^2\ V^{-1}\ s^{-1}$)[8h,9] and diffusion lengths on the order of hundreds of nanometers to micrometers in films[9a,b,10] and hundreds of micrometers for single crystals.[11] Charge-carrier lifetimes are also long, and bimolecular recombination rates defy the Langevin recombination limit by orders of magnitude.[9a]

The majority of the studies performed on perovskite solar cells and the photophysics of perovskites have been carried out at room temperature. Working solar cells, however, are exposed to various weather conditions and ambient temperatures that could easily range from –20 to 40 °C. The ambient temperature alone, however, does not determine the actual working temperature of the cell, and factors such as wind speed, panel installation angle, and heating from solar irradiance must be taken into account.[12] In a solar cell with a solar-to-electric conversion efficiency of 20% operating in an ambient temperature of 40 °C, the actual working temperature can exceed 70 °C.[12a,13]

Understanding how temperature affects the charge-carrier dynamics of perovskites is therefore essential, especially considering that the efficiency of semiconductor solar cells is known to decrease as temperature increases.[14] We focus our analysis on methylammonium lead triiodide ($CH_3NH_3PbI_3$ or $MAPbI_3$), which has become the material most frequently used in high-performing perovskite solar cells. X-ray diffraction measurements, calorimetric studies, and NMR studies have reported a

Dr. R. L. Milot, G. E. Eperon, Prof. H. J. Snaith, Prof. M. B. Johnston, Prof. L. M. Herz
Department of Physics
University of Oxford
Clarendon Laboratory
Parks Road, Oxford OX1 3PU, UK
E-mail: laura.herz@physics.ox.ac.uk

DOI: 10.1002/adfm.201502340

phase transition from tetragonal to cubic to occur at between 315 and 330 K (42–57 °C),[6,15] which is well within the range of device operating temperatures. Curiously, the cubic phase has not been widely studied in thin films, and its effect on device performance and perovskite photophysics remains unknown.

While measurements at elevated temperatures are directly applicable to devices, low-temperature measurements are also important because they can help elucidate the basic photophysical properties of the material. For example, the extent to which excitons play a role in the photoexcited carrier dynamics in perovskites has been debated in the literature. Although little evidence that excitons are present under standard operating conditions has been found,[16] binding energies ranging from 2–63 meV have been reported.[8g,i,16,17] Other localization effects, including phonon coupling and charge-carrier trapping, can also be dependent on temperature. Furthermore, $MAPbI_3$ undergoes an additional phase change from tetragonal to orthorhombic at 160 K, during which the extent of rotational freedom of the methylammonium cation is dramatically reduced.[6,8k,15a,b] All of these factors have the potential to influence the charge-carrier dynamics and thus the efficiency of charge transport within the perovskite film.

Despite the importance of temperature-dependent effects, only a few studies of the temperature dependence of the photophysics of organic–inorganic perovskites exist.[8e–k] These reports are mostly limited to the tetragonal phase. Although a few analyze the low-temperature orthorhombic phase, none of them comment on the cubic phase or analyze the dynamic processes with a time resolution better than nanoseconds. We have therefore investigated the absorption, photoluminescence (PL), recombination, mobility, and diffusion lengths of solution-processed $MAPbI_3$ thin films from temperatures ranging from 8 to 370 K using both steady-state and ultrafast spectroscopic techniques. We identify the parameters most influenced by temperature and phase changes and discuss their potential to affect solar cell performance.

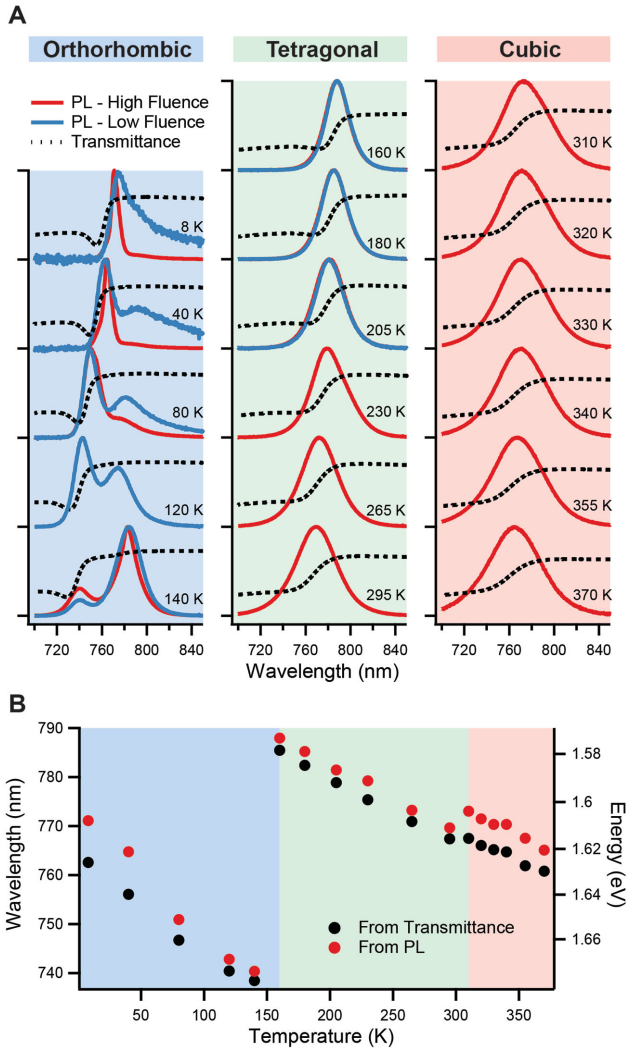

Figure 1. A) Transmittance (dashed lines) and normalized steady-state PL (solid lines) spectra of $MAPbI_3$ measured at temperatures ranging from 8 to 370 K. Black ticks on the *y*-axis indicate values of 0 and 1 below and above the respective curves. PL for both high fluences ranging from 45–120 μJ cm^{-2} (red lines) and low fluences ranging from 0.20 to 10 μJ cm^{-2} (blue lines) are included. The shading corresponds to the three different phases as labeled at the top of the figure. B) PL peak wavelength (energy) and absorption band-edge wavelength (energy) as a function of temperature. The same shading scheme is used as in part (A).

2. Results and Discussion

2.1. Band-Edge Absorption and PL

Figure 1 shows the temperature-dependent transmittance and steady-state PL measurements for a solution-processed thin film of $MAPbI_3$. A sharp decrease in transmittance associated with band-edge absorption is observed at all temperatures in the range from 730 to 790 nm. As temperature increases, this feature broadens most likely through a dominant contribution from phonon interactions.[18] At the onset of band-edge absorption, an additional peak emerges at temperatures below 180 K, which sharpens in width as the temperature is lowered to 8 K. This feature has been previously attributed to excitons,[8g,16a,19] which recent analyses suggest have a temperature-dependent binding energy as a result of a temperature-dependent dielectric constant.[8g,19] It has been proposed that above the phase transition at 160 K, the tumbling of methylammonium cations is activated,[15d] leading to a change in the dielectric function that allows for additional screening of the Coulombic interactions between electrons and holes.[19] As a result, excitons are expected to be effectively dissociated toward higher temperatures.

The wavelength of the band-edge absorption was estimated by determining the midpoint value of the transmission drop from its inflection point (Figure 1B). At 8 K, the band edge is at 763 nm and blue shifts with increasing temperature to 738 nm at 140 K. This unusual blue shift has been observed previously and has been attributed to a reverse ordering of the band edge.[1a,8j,16a,20] At 160 K, the trend changes significantly, and the band edge red shifts to 785 nm (an energy change of 100 meV). This red shift marks the phase change from the orthorhombic to the tetragonal structure and is a result of changes in methylammonium disorder and spin–orbit coupling, which both result from changes in the tilt angle of the $[PbI_6]^{4-}$ octahedra

relative to the pseudocubic framework of $CH_3NH_3^+$ ions.[6,20,21] As in the orthorhombic phase, the band edge then continues to blue shift until 310 K, where it red shifts again (by ≈5 meV). Although this energy change is more subtle, it is a clear indication of an additional change from the tetragonal to cubic phase.

The PL spectra (Figure 1A) also show significant variation with temperature and structural phase. For the tetragonal and cubic phases, trends mirror the changes in the transmission spectrum, whereas additional features are observed for the orthorhombic phase.

In the tetragonal and cubic phases, a single PL peak is observed both at high and low fluences. Its proximity to the band edge determined from the transmission measurements indicates that it is most likely due to charge-carrier recombination at the band edge, consistent with the classification of $MAPbI_3$ as a direct bandgap semiconductor.[8e] Furthermore, its shape is invariant with changes in moderate excitation fluence at constant temperature.

In the orthorhombic phase, however, differences in PL peak shape are seen both as a function of temperature and fluence. At 8 K, a sharp peak, which is slightly red shifted from the band edge, is observed with higher excitation fluence. At the lower fluence, the peak is further red shifted from the band edge and is broadened at longer wavelengths. Time-correlated single photon counting (TCSPC) measurements of the time evolution of the PL spectrum (Figure S3, Supporting Information) show that this broader feature develops within the first nanosecond following photoexcitation and is slightly longer lived than the main, peak feature. A similar fluence dependence of the steady-state PL spectra is seen at 40 K, although a clear peak is observed at longer wavelengths in addition to the broadening. This longer wavelength peak becomes more prominent with increased temperature until it is the dominant feature at 140 K.

Dual PL emission peaks appear to be a general feature in the low-temperature phase of methylammonium mixed halide lead perovskite films,[17a,22] $MAPbI_3$ single crystals,[8f] and $MAPbI_3$ films on porous TiO_2.[8g] Given the absence of a strong matching absorption onset for the lower-energy (long wavelength) feature, it has been suggested that this feature arises from a minority species.[22] The dynamic evolution of the PL spectra following photoexcitation suggests that this minority species may be fed from the majority species associated with band-edge emission,[8f,22] thus enhancing the PL in the low-energy emission peak (see Figure S3 in the Supporting Information). The predominant view in the current literature is that the low-energy emission peak arises from "trapped"[22,23] or "bound"[5a,8f] charge-carrier pairs, but the exact nature of the traps has not yet been identified. Wehrenfennig et al. proposed that such traps could arise from small inclusions of the tetragonal phase that are maintained through the phase transition into the orthorhombic phase below 160 K.[22] Such coexisting crystallographic phases have been observed in inorganic perovskite materials and may arise, e.g., from strain imposed by the substrate on the perovskite film.[24] Baikie et al. have suggested that a continuous structural transition between the tetragonal and orthorhombic phases of $MAPbI_3$ is impossible,[6] which may trigger the formation of these inclusions. Future work identifying the nature of trap states in the low-temperature phase is clearly required. In the meantime, our further analysis of the PL emission will focus on the band-edge emission associated with intrinsic charge-carrier pairs.

Figure 1B compares the wavelengths and energies of the PL maxima to the band edges determined from the transmittance spectra. As compared to the band-edge absorbance, the PL peak is slightly red shifted with respect to the absorption onset midpoint across the entire temperature range investigated. In the tetragonal phase, this Stokes shift is a constant, 4–6 meV, whereas the shift is greater (11–12 meV) in the cubic phase. One explanation for this shift is the presence of trap states below the band edge, although polaronic effects may also contribute.[18,25] The PL spectra (Figure 1A) are also significantly broadened upon entry into the cubic phase, consistent with a stronger presence of inhomogeneity. Trap states have been previously observed in perovskite films and have been found to be particularly sensitive to film fabrication and deposition substrate.[16a,23,26] Our observations suggest that the energetics of the trap states are also significantly affected by phase transitions (vide infra), which most likely derive from the associated alteration in electronic band structure that may lead to different energy offsets between band edges and trap levels.

Although the PL is still red shifted with respect to the band edge, the behavior in the orthorhombic phase is slightly different than in the two higher temperature phases. Toward lower temperatures, the PL peak and absorption edge energies diverge, with the Stokes shift increasing from 4 meV at 140 K to nearly 18 meV at 8 K. As we demonstrate below, charge carriers exhibit an increasing localization response toward lower temperature for this range. Therefore, the observed deviation in behavior toward the lowest temperatures may be associated with an increasing presence of excitons.

2.2. Recombination Dynamics

An understanding of what governs charge-carrier recombination is highly important as recombination competes with efficient charge collection in a solar cell. A range of different charge-carrier recombination mechanisms exist, which depend on the charge-carrier density n to a different degree, and the rate of change in n can be expressed through the following equation:

$$\frac{dn}{dt} = -k_3 n^3 - k_2 n^2 - k_1 n \tag{1}$$

where k_1 is the monomolecular recombination rate constant (which is typically related to charge trapping), k_2 is the bimolecular (electron–hole) recombination rate constant, and k_3 is the third-order Auger rate constant.[9a] In the following, we unravel how the observed changes in phase affect the charge-carrier recombination dynamics in $MAPbI_3$.

To determine k_1, time-resolved PL decay measurements were taken at the PL peak wavelengths following excitation at 405 nm (see Figure S4 in the Supporting Information). For instances where two PL peaks were observed, only the dynamics for the higher energy peak were considered. The excitation fluence (6 nJ cm^{-2}) was selected such that the long time PL dynamics were independent of the excitation fluence in order to ensure

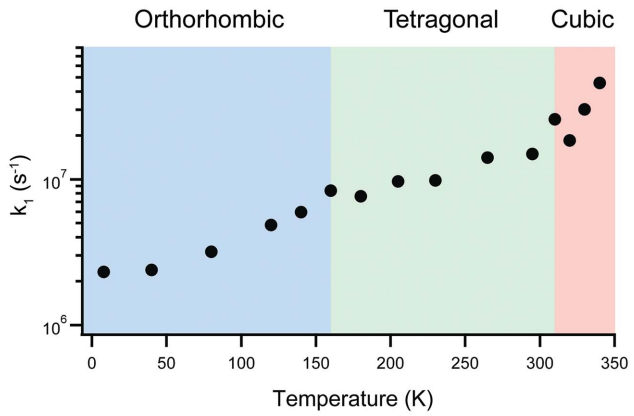

Figure 2. The temperature dependence of the monomolecular recombination rate, k_1. Values are provided in Table S1 (Supporting Information).

that monomolecular recombination processes were dominant. An exponential function was then fit to the decay dynamics to extract k_1.

As seen in **Figure 2**, k_1 increases with increasing temperature from 2.3×10^6 s^{-1} at 8 K to 4.6×10^7 s^{-1} at 340 K. The rate of change with temperature is fairly constant in the orthorhombic and tetragonal phases but accelerates in the cubic phase. The general trend of increasing monomolecular recombination rate with increasing temperature is consistent with a charge-recombination process assisted by ionized impurities. Traps for either electrons or holes in $MAPbI_3$ may originate from a wide variety of sources, including elemental vacancies, substitutions, or interstitials.[27] Recent DFT calculations have suggested that shallow traps are easier to form than deeper traps,[27a] in agreement with the generally low values of k_1 we observe. As the temperature is reduced below the ionization energy associated with the impurity, the released electrons or holes return, thus effectively passivating this site. At low temperature, such unintentional doping is therefore "frozen out" reducing dopant site assisted recombination.[28] We are therefore able to extract a value for the ionization energy of such sites from an Arrhenius analysis, which can be viewed as the "trap depth" for the affected charge carrier (electron or hole) with respect to their relevant band edge (conduction band minimum or valence band maximum).

Our analysis reveals that these relative trap depths depend significantly on the crystal structure. Arrhenius plots of the tetragonal and cubic phases (Figure S5, Supporting Information) are linear, yielding activation energies of 20 and 200 meV, respectively, which are both within the range of trap state energy levels reported previously in experimental and computational studies.[23,27] The difference in activation energies suggests that the relative band alignment of the impurity states are markedly different in the cubic and tetragonal phases, which is consistent with our previous observation of an increased Stokes shift in the PL from the cubic phase.

Unlike in the high-temperature phases, a linear Arrhenius plot was not obtained for the orthorhombic phase, as the rate approaches a constant value toward lower temperatures. As the overall monomolecular recombination rate can be accelerated by processes such as exciton binding, phonon coupling, or exciton self-trapping,[25] this nonlinear behavior adds to the evidence for increasing charge-carrier localization at low temperatures.

The higher order rate constants, k_2 and k_3, were determined using optical-pump–THz probe spectroscopy. Measurements of the change in terahertz (THz) transmission, $\Delta T/T$, as a function of the time delay between a 550 nm optical pump pulse and THz probe pulse were made in order to obtain the carrier decay dynamics. The value of $\Delta T/T$ is proportional to the change in conductivity upon photoexcitation and is thus proportional to the carrier mobility times the carrier density.[29] The decay of $\Delta T/T$ as a function of time within the 1.5 ns window is attributed to charge-carrier recombination.[9a]

Figure 3, which displays fluence-dependent THz data at representative temperatures in each phase, reveals stark

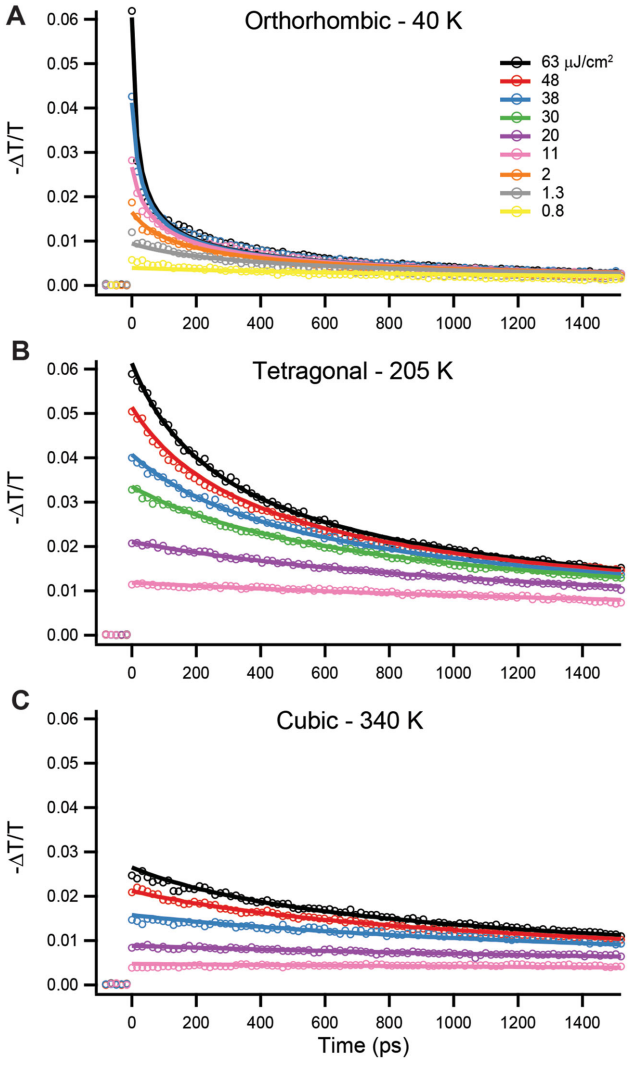

Figure 3. Recombination dynamics measured by optical-pump–THz probe spectroscopy at representative temperatures in each of the three phases of $MAPbI_3$: A) orthorombic at 40 K, B) tetragonal at 205 K, and C) cubic at 340 K. The $MAPbI_3$ thin film was photoexcited at 550 nm with fluences ranging from 0.8 to 63 μJ cm^{-2}. Open circles represent experimental data, and solid lines are fits to Equation (1). The legend in part (A) also applies to parts (B) and (C).

differences in the higher order recombination dynamics with changes in temperature and phase. The one common feature is that the dynamics are highly fluence dependent, which is characteristic behavior for second- and third-order processes. As the fluence decreases, the dynamics flatten as monomolecular processes, which occur on a much longer timescale than the ≈1.5 ns timescale of the experiment, dominate. Despite this similarity, striking differences in the decay dynamics are apparent in the three phases. At 40 K (orthorhombic phase), the dynamics are fastest, and monomolecular processes dominate only below 0.8 μJ cm^{-2}. In contrast, the tetragonal and cubic phases show slower dynamics and flatten at much higher fluences (≈10 μJ cm^{-2}), suggesting both increased monomolecular rates and decreased higher order rates. A decrease in mobility in the cubic phase is evidenced by a smaller initial value of $\Delta T/T$ at comparable fluences.

The bimolecular and Auger recombination rate constants were extracted by fitting Equation (1) to the transient THz data. At each temperature, the data were fit globally across the range of fluences investigated, and k_1 was fixed at the value obtained from TCSPC measurements. Further details of the fitting procedure can be found in the Supporting Information.

The bimolecular rate constant k_2, which is associated with recombination between electrons in the conduction band and holes in the valence band, is shown in **Figure 4**A. Unlike k_1, the bimolecular recombination constant increases toward lower temperatures and does not change significantly at the phase transitions. One commonly evoked benchmark for bimolecular recombination rates is the Langevin model, which assumes that electron–hole recombination will occur once the two charges have moved within a joint Coulomb capture radius out of which thermally activated escape is no longer likely.[30] While the Langevin model has been shown to overestimate the value of k_2 for lead-halide perovskites,[17,30] it generally predicts a decrease in k_2 with decreasing charge-carrier mobility as a reduced mobility will lead to a decrease in the approach velocity of an electron into the hole's Coulombic capture radius. As we show below, the charge-carrier mobility is indeed found to decrease with increased temperature, thereby mirroring the trends observed for k_2. Therefore, we demonstrate that despite the strong reduction in the bimolecular recombination with respect to values expected from Langevin theory, its broad predicted trend still appears to hold.

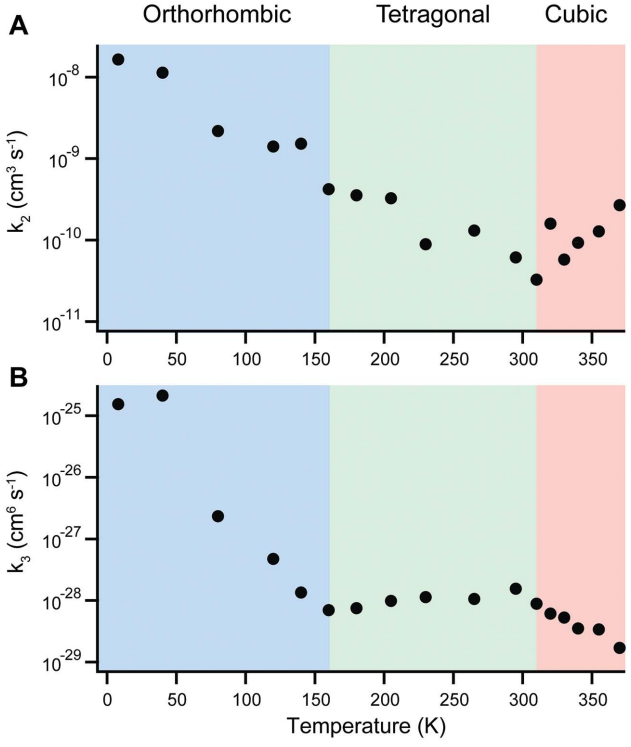

Figure 4. Temperature dependence of A) the bimolecular and B) Auger recombination rate constants obtained for $MAPbI_3$. Values are provided in Table S1 (Supporting Information).

While Auger recombination may not be significant at the charge-carrier concentrations present in solar cells under standard AM1.5 illumination, it is likely to play a strong role in laser or solar-concentrator applications. Figure 4B shows the temperature dependence of the associated Auger recombination rate constant k_3, which is found to exhibit significant phase specificity. Whereas it decreases by more than four orders of magnitude in the orthorhombic phase, it increases by a factor of three in the tetragonal phase, and decreases by an additional order of magnitude in the cubic phase.

Auger recombination in semiconductors is highly influenced by the requirement of overall energy and momentum conservation in the many-body process. One consequence is a high dependence of the Auger rate constant on the electronic band structure.[31] DFT calculations predict significant changes in the band structure of $MAPbI_3$ with changes in crystal structure due to varying degrees of spin-orbit coupling and hydrogen bonding.[5a,c,21,32] Efficient Auger recombination may, e.g., result from the involvement of split-off bands that facilitate energy and wavevector conservation.[33] In $MAPbI_3$, such mechanisms differ subtly from those in traditional semiconductors such as GaAs due to the reverse ordering of the band structure involving the split-off and light/heavy electron conduction bands.[20] In GaSb, such effects yield an unusual temperature dependence in which the rate increases with increasing temperature to 95 K and then begins to decrease toward higher temperature.[33] While these results somewhat mirror the trends observed in the tetragonal and cubic phases for $MAPbI_3$, they do not explain the discontinuities in temperature gradient at the phase transitions. Auger recombination rate constants can also be greatly affected by impurities,[34] which our measurements suggest are also altered by structural phase changes. Furthermore, phonons can play a role, in particular by accepting or donating momentum, and will impart a strong temperature dependence.[34a,b] Our first observations of Auger rate constants in $MAPbI_3$, across a temperature range spanning the three different structural phases will allow the detailed theoretical analysis of what constitutes Auger mechanisms in these materials. Such an understanding is urgently needed for the use of these materials for lasing applications, as the charge densities required for population inversion are in a regime for which Auger recombination is dominant.[5a,c]

2.3. Charge Transport

Previous measurements of the frequency-domain THz spectra of perovskites have shown that the conductivity in $MAPbI_{3-x}Cl_x$ and $MAPbI_3$ films obeys the classical Drude model[9a,b] similar to what is expected for high-quality inorganic semiconductors with long momentum scattering times for charge carriers. These results are in contrast to many nano- and polycrystalline semiconductor films, for which localization at grain boundaries can significantly limit the conductivity.[29a] With changing temperature, differences in exciton binding or phonon coupling can also limit the conductivity and give rise to analogous localization effects.

To examine whether the Drude model appropriately describes the conductivity for all phases and temperatures, THz photoconductivity spectra were collected at 5 ps after photoexcitation (**Figure 5** and Figure S6, Supporting Information). At room temperature (Figure 5A), a characteristic Drude response is observed. The real part of the conductivity is constant from 0.5 to 3.5 THz, and the imaginary part is near zero. Some evidence of phonon coupling is also observed, as weak features are present near 1 and 2 THz at the phonon frequencies for the nonphotoexcited material.[9b] The coupling, however, does not appear to interfere with the overall Drude response of the material. Similar spectra are obtained at temperatures throughout the tetragonal and cubic phases (Figure S6, Supporting Information). At temperatures in the orthorhombic phase, however, the spectra are increasingly influenced by phonon modes, which is evidenced by the features observed below 2 THz (Figure 5B). The features observed in this spectral window sharpen with decreasing temperature and are associated with lead-iodide vibrational modes.[35] Additionally, the amplitude of the real component begins to decrease toward higher frequencies, and the imaginary component becomes nonzero.

In order to quantify these deviations from the Drude model, Equation (2) defines a Drude quality factor f_{Drude}

$$f_{\text{Drude}} = \frac{1}{x}\sum_{1}^{x}\frac{\sqrt{(\text{Re}(\Delta T/T))^2}}{\sqrt{(\text{Im}(\Delta T/T))^2+(\text{Re}(\Delta T/T))^2}} \quad (2)$$

Here, $\Delta T/T$ is the change in THz transmission at each frequency point and x is the total number of points. Values of 1 indicate ideal Drude behavior, and values less than 1 indicate the extent of deviations from ideality.

In the tetragonal and cubic phases, f_{Drude} is nearly 1, indicating that the conductivity obeys the Drude model. Below the tetragonal to orthorhombic phase transition temperature, however, deviations from ideal Drude behavior are apparent. Furthermore, the extent of deviation increases as the temperature decreases. These results provide evidence of charge-carrier localization at low temperature and are consistent with the emergence of excitonic effects at temperatures below the phase transition at 160 K. They further suggest that the predominant species in this material for temperatures above ≈80 K are free charge-carrier pairs, with excitons only contributing to a significant extent at temperatures below 80 K.

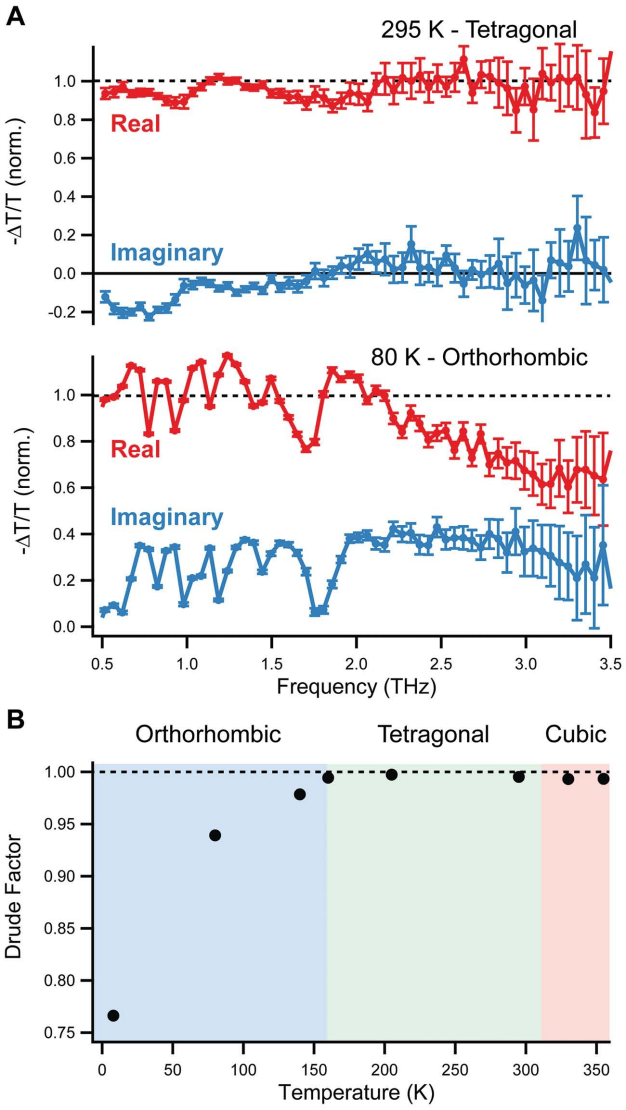

Figure 5. A) Frequency-dependent THz spectra measured at 295 and 80 K. The sample was photoexcited at 550 nm, and spectra were taken at a pump delay time of 5 ps. The real part of the conductivity is shown in red, and the imaginary part is in blue. B) Drude factor calculated according to Equation (2). Additional THz spectra are included in Figure S6 (Supporting Information).

2.4. Carrier Mobility and Diffusion Length

Our studies demonstrate that carrier dynamics are highly dependent on crystal phase. However, these observations pose the important question of to what extent these parameters affect device performance. We therefore evaluate the charge-carrier mobility and carrier-diffusion length, focusing more specifically on temperatures relevant to device operation.

Since the optical-pump–THz probe differential transmission signal (Figure 3) is proportional to the photoinduced conductivity, the charge-carrier mobility μ can be extracted with knowledge of the initially generated carrier density N and experimental parameters (see the Supporting Information). It is important to note that N depends on the photon-to-charge

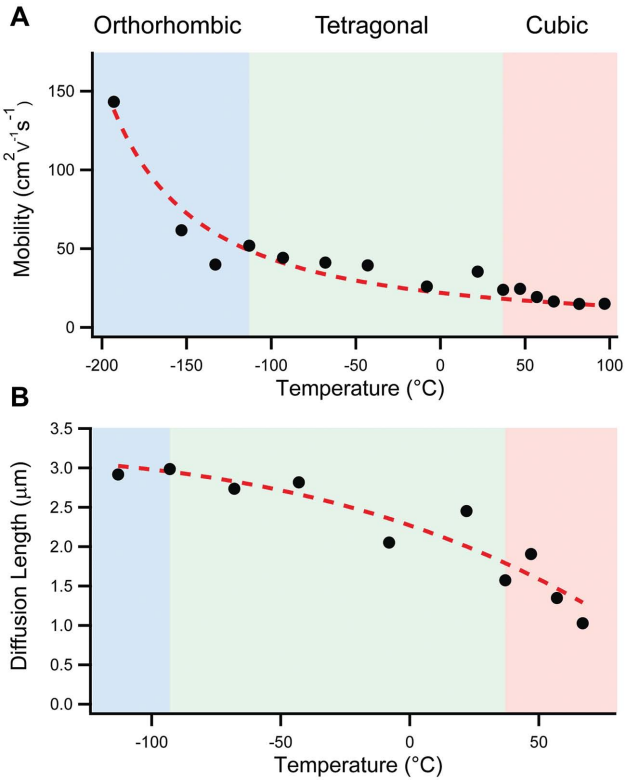

Figure 6. A) Mobility determined from optical-pump–THz probe measurements. Values are tabulated in Table S1 in the Supporting Information. The black dots represent data, and the dashed line is the theoretical $T^{-3/2}$ dependence predicted for band-like transport. B) Diffusion lengths (black dots) at possible cell working temperatures. The dashed line is a guide to the eye.

branching ratio φ, which is the fraction of free carriers generated per incoming photon. However, for the temperature range examined here (≥80 K) the conductivity is Drude-like (see Figure 5B), and we therefore reasonably assume the photon-to-charge branching ratio to be 1.

Figure 6A displays the extracted charge-carrier mobility as a function of temperature. The room temperature mobility was determined to be 35 cm^2 V^{-1} s^{-1}, which is comparable with previous measurements.[9a,c] Across all three phases, the mobility decreases with increasing temperature as previously found for the tetragonal phase.[8h,i] The dashed red line in Figure 6A represents the theoretical temperature dependence of the mobility assuming band-like transport limited only by scattering off phonons.[8h,i] For the most part, our experimental values follow this $T^{-3/2}$ dependence without any significant discontinuities at the phase transitions, reaching a value of 150 cm^2 V^{-1} s^{-1} at –193 °C (80 K).

Within the Drude model, the charge-carrier mobility μ of an electron or hole depends on both momentum scattering time τ and the effective mass m^* according to $\mu = e\tau/m^*$. It has been suggested that the effective mass of charge-carrier pairs changes very little upon the transition from the tetragonal to the orthorhombic phase.[36] The surprising absence of sudden changes in charge-carrier mobility across the phase transition we report here suggests that the momentum scattering time is also hardly affected by the strong changes in the electronic structure occurring upon the phase transitions. These findings, in conjunction with the $T^{-3/2}$ dependence of the charge-carrier mobility, suggest that charge-carrier interactions with the phonon bath are relatively unchanged through the structural phase transitions.

We find that the mobility remains relatively high even above room temperature and upon entry into the cubic phase. As Figure 6B shows, between room temperature (22 °C) and 100 °C, the charge-carrier mobility decreases gradually from ≈30 to 15 cm^2 V^{-1} s^{-1}. Despite this decrease, the mobility remains in the range of room-temperature values reported for perovskites processed under different conditions,[9] which suggests that device performance at higher temperatures will not be severely limited by slightly impeded carrier transport.

In order to further investigate the effects of mobility and recombination rate changes in the range of temperatures possible under cell operating conditions, diffusion lengths L_D were calculated according to Equation (3)

$$L_D(n) = \sqrt{\frac{D}{R_{total}(n)}} \tag{3}$$

The total recombination rate R_{total} is determined by the carrier density and the recombination rate constants (k_1, k_2, and k_3) of the individual recombination processes

$$R_{total} = -\frac{1}{n}\frac{dn}{dt} = n^2k_3 + nk_2 + k_1 \tag{4}$$

Here, the diffusion constant D is the product of the mobility μ, Boltzmann constant k_B, and temperature T divided by the elementary charge e

$$D = \frac{\mu k_B T}{e} \tag{5}$$

Values of the diffusion length for temperatures ranging from –113 to 67 °C are shown in Figure 6B. A carrier density of 10^{-14} cm^{-3} was used for the calculations as a value typical under standard device operating conditions.[16a] Over this temperature range, the diffusion length decreases from about 3 μm at –93 °C to 2.5 μm at 22 °C and to 1.2 μm at 67 °C. Since the calculations were performed at a low carrier density, the effects of bimolecular and Auger recombination are relatively small, and the monomolecular recombination rate and mobility determine the diffusion length (a discussion of charge diffusion at higher carrier densities is included in the Supporting Information). From –43 to 67 °C, the mobility decreases by about a factor of two, and k_1 increases by nearly a factor of 5. The decrease in diffusion length with increased temperature is thus due largely to the increase in k_1. These results suggest that high-temperature photovoltaic device operations would mostly benefit from a reduction in impurity concentration. That said, at all temperatures investigated, the diffusion length remains significantly above the absorption depth of light across the visible spectrum (0.66 μm in $MAPbI_3$ for 550 nm light).[1b] Therefore, our result demonstrates that there are no fundamental obstacles to the operation of $MAPbI_3$ photovoltaics at elevated temperatures typical in field usage.

3. Conclusion

We have evaluated the PL, transmittance, charge-carrier recombination dynamics, mobility, and diffusion length for $MAPbI_3$ in the temperature range from 8 to 370 K across two structural phase transitions. Our results allow us to unravel the complex contributions to the remarkable materials properties that have contributed to the success in photovoltaic applications.

A combined analysis of absorption, PL, and THz conductivity spectra enabled the elucidation of the effects of excitonic contributions as a function of temperature. Typical for direct bandgap semiconductors, it is expected that Coulomb correlations enhance the electronic transitions in $MAPbI_3$ across a given temperature range. However, clear evidence for localization effects associated with the formation of excitonic states is only found at temperatures below 80 K. Above this temperature, THz conductivity spectra are Drude-like in accordance with the presence of free charge carriers. These results therefore support an emerging picture of excitonic effects being mostly dominant in the low-temperature orthorhombic phase, where the dielectric screening may be reduced by freezing of methylammonium cation motion.[8g,19,37]

Analysis of the temperature-dependent charge-carrier recombination reveals a variety of starkly differing recombination mechanisms. The monomolecular rate is found to increase with temperature in accordance with what would be expected for a mechanism based on impurity-assisted recombination. As the temperature is reduced, dopant charges return to their ionized impurities, effectively passivating these recombination centers. Surprisingly different values are obtained for the room-temperature tetragonal (20 meV) and the higher-temperature cubic (200 meV) phase. While the bandgap energy appears to show only very subtle shifts upon entry into the cubic phase, an accompanying shift in the relative energy alignment of bands to trap states appears to be the most prominent effect. These observations may help with the identification of these trap states, whose origin and nature still remains a matter of debate.

Higher-order recombination effects present markedly different dependence on temperature, with the bimolecular recombination rate constant decreasing as temperature is increased. This trend can be conceptually understood in the context of a charge-carrier mobility that is decreasing with increasing temperature as a result of electron–phonon interactions. In the general concept of Langevin recombination, the bimolecular recombination between free electrons and free holes is influenced by their average velocity of approach into the Coulomb capture radius, and therefore expected to reduce with decreasing charge-carrier mobility.

The dependence of Auger (third-order) recombination shows exceptionally strong phase specificity, suggesting a clear link with electronic and/or vibrational structure. While Auger recombination is insignificant for operation of photovoltaic cells at standard solar illumination intensities, it is likely to play a crucial role for the development of lasers based on organic–inorganic perovskites. For the charge-carrier density thresholds of $\approx 10^{18}$ cm^{-3} reported for amplified spontaneous emission from related materials, Auger recombination will unfortunately already form the majority of the overall recombination rate R_{total} for $MAPbI_3$ at room temperature. However, our observations suggest that suitable band-structure engineering (e.g., through changes in organic cation size) may reduce these rates dramatically. A better understanding of Auger mechanisms, perhaps through modeling these data with density functional theory, may be a promising avenue for further research.

Finally, we use our findings to make predictions on how device operation at elevated temperatures is likely to be affected across the tetragonal-to-cubic phase transition where photovoltaic devices are likely to operate in field usage. The charge-carrier diffusion length gradually decreases with increasing temperature from about 3 µm at –93 °C to 1.2 µm at 67 °C. While these changes are partly caused by a largely unavoidable decrease in charge-carrier mobility, a more significant contribution is the increase in charge-carrier trapping rates upon entry into the cubic phase, which should be controllable with better processing procedures. Across the range of typical solar cell operating temperatures, however, the charge-carrier diffusion length remains well above the optical absorption depth in the visible spectrum, revealing that there are no fundamental obstacles to the operation of cells based on $MAPbI_3$ under typical field conditions.

4. Experimental Section

Thin-Film Fabrication: All materials for $MAPbI_3$ film fabrication were purchased from Sigma-Aldrich and used as received. Methylammonium iodide (MAI) was synthesized in-house following a published procedure.[3] Films were prepared on z-cut quartz substrates, which were initially cleaned with acetone followed by propan-2-ol and then treated with oxygen plasma. Perovskite films were deposited in a nitrogen-filled glovebox using a 'solvent quenching' method as described previously.[38] A 1:1 molar ratio of CH_3NH_3I (MAI) and PbI_2 was dissolved in anhydrous *N*,*N*-dimethylformamide to form a 0.88 M solution. This solution was then spin-coated onto the quartz substrates at 5000 rpm for 25 s. After 7 s of spin-coating, an excess of anhydrous chlorobenzene was rapidly deposited onto the spinning film. The resulting films were then annealed at 100 °C for 10 min. This procedure produces ≈400 nm thick perovskite films with very uniform and smooth morphology. Additional film characterization information is provided in the Supporting Information.

Visible/NIR Spectroscopy: Temperature-dependent visible/NIR transmission measurements were performed using a Fourier-transform infrared spectrometer (Bruker, Vertex 80v). Spectra were taken using a tungsten halogen lamp source and a silicon diode detector. The sample and a bare z-cut quartz substrate were mounted in a cold-finger cryostat (MicrostatHe, Oxford Instruments) and the temperature was controlled with liquid helium and an accompanying temperature controller (ITC503, Oxford Instruments). The temperature was monitored with sensors mounted both on the cryostat heat exchanger and at the end of the sample holder. Measurements of both the $MAPbI_3$ sample and the quartz reference were taken in the increments of 10–30 °C from 8 to 370 K, which is below the temperature where $MAPbI_3$ begins to decompose.[1c]

Time-Correlated Single Photon Counting: For time-resolved PL, a picosecond pulsed diode laser (Picoquant, LDH-D-C-405M) centered at 405 nm and with a repetition rate of 5 MHz was used to photoexcite the sample. The PL was collected and directed toward a grating monochromator (Princeton Instruments, SP-2558) fitted with a photon-counting detector (PDM series from MPD). The timing was controlled with a PicoHarp300 TCSPC event timer, giving an instrument response time of ≈1 ns at the used sampling rate. The samples were mounted in the cryostat, and time decay traces, which were measured at the maximum PL wavelength, were recorded at fluences ranging from 0.023 µJ cm^{-2} to 1.02 µJ cm^{-2} at

each temperature point. Full spectra were also obtained at select temperatures.

Optical-Pump–THz Probe (OPTP) Spectroscopy: The output of an amplified laser (Mai Tai–Empower–Spitfire Pro from Spectra Physics) with an 800 nm center wavelength, a 35 fs pulse duration, and a 5 kHz repetition rate was used to generate THz radiation via optical rectification in a 2 mm thick GaP(110) crystal and detect it via electrooptic sampling with a 0.2 mm thick GaP(110) crystal and a pair of balanced photodiodes. The THz radiation was focused onto the samples, which were mounted on the cryostat cold finger, and photoexcited using the output of an optical parametric amplifier (TOPAS-C, Spectra Physics) tuned to 550 nm. To obtain the photoconductivity dynamics, the broadband change in transmitted THz radiation (peak time-domain amplitude) was monitored as a function of the delay time between the optical pump pulse and THz probe pulse. For all temperatures, decay traces were recorded at several fluences between 0.20 μJ cm^{-2} and 121 μJ cm^{-2}. In addition, full THz time-domain spectra were collected at fixed pump delay times following photoexcitation. More details about the THz spectrometer and data collection procedures can be found in Ref. [39] In conjunction with the THz measurements, in situ steady-state PL spectra were collected at identical temperatures and fluences using a UV–vis mini spectrometer (Ocean Optics, USB2000+) fitted with an optical fiber and a collimating lens.

Supporting Information

Supporting Information is available from the Wiley Online Library or from the author.

Acknowledgements

The authors thank the Engineering and Physical Sciences Research Council (EPSRC) for financial support.

Received: June 9, 2015
Revised: July 24, 2015
Published online: September 15, 2015

[1] a) M. A. Green, A. Ho-Baillie, H. J. Snaith, *Nat. Photon.* **2014**, *8*, 506; b) H. S. Jung, N. G. Park, *Small* **2015**, *11*, 10; c) B. H. Wang, X. D. Xiao, T. Chen, *Nanoscale* **2014**, *6*, 12287; d) H. J. Snaith, *J. Phys. Chem. Lett.* **2013**, *4*, 3623; e) P. Gao, M. Grätzel, M. K. Nazeeruddin, *Energy Environ. Sci.* **2014**, *7*, 2448; f) S. Brittman, G. W. P. Adhyaksa, E. C. Garnett, *MRS Commun.* **2015**, *5*, 7.

[2] a) A. Kojima, K. Teshima, Y. Shirai, T. Miyasaka, *J. Am. Chem. Soc.* **2009**, *131*, 6050; b) H. S. Kim, C. R. Lee, J. H. Im, K. B. Lee, T. Moehl, A. Marchioro, S. J. Moon, R. Humphry-Baker, J. H. Yum, J. E. Moser, M. Grätzel, N. G. Park, *Sci. Rep.* **2012**, *2*, 591.

[3] M. M. Lee, J. Teuscher, T. Miyasaka, T. N. Murakami, H. J. Snaith, *Science* **2012**, *338*, 643.

[4] a) M. A. Green, K. Emery, Y. Hishikawa, W. Warta, E. D. Dunlop, *Prog. Photovoltaics* **2015**, *23*, 1; b) W. S. Yang, J. H. Noh, N. J. Jeon, Y. C. Kim, S. Ryu, J. Seo, S. I. Seok, *Science* **2015**, *348*, 1234.

[5] a) G. C. Xing, N. Mathews, S. S. Lim, N. Yantara, X. F. Liu, D. Sabba, M. Grätzel, S. Mhaisalkar, T. C. Sum, *Nat. Mater.* **2014**, *13*, 476; b) S. D. Stranks, S. M. Wood, K. Wojciechowski, F. Deschler, M. Saliba, H. Khandelwal, J. B. Patel, S. J. Elston, L. M. Herz, M. B. Johnston, A. P. H. J. Schenning, M. G. Debije, M. K. Riede, S. M. Morris, H. J. Snaith, *Nano Lett.* **2015**, *15*, 4935; c) F. Deschler, M. Price, S. Pathak, L. E. Klintberg, D. D. Jarausch, R. Higler, S. Huttner, T. Leijtens, S. D. Stranks, H. J. Snaith, M. Atature, R. T. Phillips, R. H. Friend, *J. Phys. Chem. Lett.* **2014**, *5*, 1421.

[6] T. Baikie, Y. N. Fang, J. M. Kadro, M. Schreyer, F. X. Wei, S. G. Mhaisalkar, M. Grätzel, T. J. White, *J. Mater. Chem. A* **2013**, *1*, 5628.

[7] M. Z. Liu, M. B. Johnston, H. J. Snaith, *Nature* **2013**, *501*, 395.

[8] a) M. R. Filip, G. E. Eperon, H. J. Snaith, F. Giustino, *Nat. Commun.* **2014**, *5*, 5757; b) G. E. Eperon, S. D. Stranks, C. Menelaou, M. B. Johnston, L. M. Herz, H. J. Snaith, *Energy Environ. Sci.* **2014**, *7*, 982; c) N. K. Noel, S. D. Stranks, A. Abate, C. Wehrenfennig, S. Guarnera, A. A. Haghighirad, A. Sadhanala, G. E. Eperon, S. K. Pathak, M. B. Johnston, A. Petrozza, L. M. Herz, H. J. Snaith, *Energy Environ. Sci.* **2014**, *7*, 3061; d) P. P. Boix, S. Agarwala, T. M. Koh, N. Mathews, S. G. Mhaisalkar, *J. Phys. Chem. Lett.* **2015**, *6*, 898; e) Y. Yamada, T. Nakamura, M. Endo, A. Wakamiya, Y. Kanemitsu, *Appl. Phys. Express* **2014**, *7*, 032302; f) H.-H. Fang, R. Raissa, M. Abdu-Aguye, S. Adjokatse, G. R. Blake, J. Even, M. A. Loi, *Adv. Funct. Mater.* **2015**, *25*, 2378; g) Y. Yamada, T. Nakamura, M. Endo, A. Wakamiya, Y. Kanemitsu, *IEEE J. Photovoltaics* **2015**, *5*, 401; h) H. Oga, A. Saeki, Y. Ogomi, S. Hayase, S. Seki, *J. Am. Chem. Soc.* **2014**, *136*, 13818; i) T. J. Savenije, C. S. Ponseca, L. Kunneman, M. Abdellah, K. B. Zheng, Y. X. Tian, Q. S. Zhu, S. E. Canton, I. G. Scheblykin, T. Pullerits, A. Yartsev, V. Sundström, *J. Phys. Chem. Lett.* **2014**, *5*, 2189; j) T. Ishihara, *J. Lumin.* **1994**, *60-1*, 269; k) A. Maalej, Y. Abid, A. Kallel, A. Daoud, A. Lautie, F. Romain, *Solid State Commun.* **1997**, *103*, 279.

[9] a) C. Wehrenfennig, G. E. Eperon, M. B. Johnston, H. J. Snaith, L. M. Herz, *Adv. Mater.* **2014**, *26*, 1584; b) C. Wehrenfennig, M. Z. Liu, H. J. Snaith, M. B. Johnston, L. M. Herz, *Energy Environ. Sci.* **2014**, *7*, 2269; c) C. S. Ponseca, T. J. Savenije, M. Abdellah, K. B. Zheng, A. Yartsev, T. Pascher, T. Harlang, P. Chabera, T. Pullerits, A. Stepanov, J. P. Wolf, V. Sundström, *J. Am. Chem. Soc.* **2014**, *136*, 5189.

[10] S. D. Stranks, G. E. Eperon, G. Grancini, C. Menelaou, M. J. P. Alcocer, T. Leijtens, L. M. Herz, A. Petrozza, H. J. Snaith, *Science* **2013**, *342*, 341.

[11] Q. F. Dong, Y. J. Fang, Y. C. Shao, P. Mulligan, J. Qiu, L. Cao, J. S. Huang, *Science* **2015**, *347*, 967.

[12] a) E. Skoplaki, A. G. Boudouvis, J. A. Palyvos, *Sol. Energy Mater. Sol. Cells* **2008**, *92*, 1393; b) E. Skoplaki, J. A. Palyvos, *Sol. Energy* **2009**, *83*, 614.

[13] R. G. Ross Jr., in *Proc. Fourteenth IEEE Photovoltaic Specialists Conf.*, IEEE, Picastaway, NJ, USA **1980**, p. 1126.

[14] J. Nelson, *The Physics of Solar Cells*, Imperial College Press, London, UK **2003**.

[15] a) Y. Kawamura, H. Mashiyama, K. Hasebe, *J. Phys. Soc. Jpn.* **2002**, *71*, 1694; b) N. Onoda-Yamamuro, T. Matsuo, H. Suga, *J. Phys. Chem. Solids* **1990**, *51*, 1383; c) R. E. Wasylishen, O. Knop, J. B. Macdonald, *Solid State Commun.* **1985**, *56*, 581; d) A. Poglitsch, D. Weber, *J. Chem. Phys.* **1987**, *87*, 6373.

[16] a) V. D'Innocenzo, G. Grancini, M. J. P. Alcocer, A. R. S. Kandada, S. D. Stranks, M. M. Lee, G. Lanzani, H. J. Snaith, A. Petrozza, *Nat. Commun.* **2014**, *5*, 3586; b) Q. Q. Lin, A. Armin, R. C. R. Nagiri, P. L. Burn, P. Meredith, *Nat. Photonics* **2015**, *9*, 106.

[17] a) K. W. Wu, A. Bera, C. Ma, Y. M. Du, Y. Yang, L. Li, T. Wu, *Phys. Chem. Chem. Phys.* **2014**, *16*, 22476; b) K. Tanaka, T. Takahashi, T. Ban, T. Kondo, K. Uchida, N. Miura, *Solid State Commun.* **2003**, *127*, 619; c) M. Hirasawa, T. Ishihara, T. Goto, K. Uchida, N. Miura, *Physica B* **1994**, *201*, 427.

[18] C. Wehrenfennig, M. Z. Liu, H. J. Snaith, M. B. Johnston, L. M. Herz, *J. Phys. Chem. Lett.* **2014**, *5*, 1300.

[19] J. Even, L. Pedesseau, C. Katan, *J. Phys. Chem. C* **2014**, *118*, 11566.

[20] J. Even, L. Pedesseau, C. Katan, M. Kepenekian, J.-S. Lauret, D. Sapori, E. Deleporte, *J. Phys. Chem. C* **2015**, *119*, 10161.

[21] J. Even, L. Pedesseau, J. M. Jancu, C. Katan, *Phys. Status Solidi-Rapid Res. Lett.* **2014**, *8*, 31.

[22] C. Wehrenfennig, M. Z. Liu, H. J. Snaith, M. B. Johnston, L. M. Herz, *APL Mater.* **2014**, *2*, 081513.
[23] X. X. Wu, M. T. Trinh, D. Niesner, H. M. Zhu, Z. Norman, J. S. Owen, O. Yaffe, B. J. Kudisch, X. Y. Zhu, *J. Am. Chem. Soc.* **2015**, *137*, 2089.
[24] a) L. Ehm, L. A. Borkowski, J. B. Parise, S. Ghose, Z. Chen, *Appl. Phys. Lett.* **2011**, *98*, 021901; b) R. J. Zeches, M. D. Rossell, J. X. Zhang, A. J. Hatt, Q. He, C. H. Yang, A. Kumar, C. H. Wang, A. Melville, C. Adamo, G. Sheng, Y. H. Chu, J. F. Ihlefeld, R. Erni, C. Ederer, V. Gopalan, L. Q. Chen, D. G. Schlom, N. A. Spaldin, L. W. Martin, R. Ramesh, *Science* **2009**, *326*, 977.
[25] R. T. Williams, K. S. Song, *J. Phys. Chem. Solids* **1990**, *51*, 679.
[26] a) T. Leijtens, S. D. Stranks, G. E. Eperon, R. Lindblad, E. M. J. Johansson, I. J. McPherson, H. Rensmo, J. M. Ball, M. M. Lee, H. J. Snaith, *ACS Nano* **2014**, *8*, 7147; b) Y. Yamada, T. Nakamura, M. Endo, A. Wakamiya, Y. Kanemitsu, *J. Am. Chem. Soc.* **2014**, *136*, 11610; c) V. D'Innocenzo, A. R. S. Kandada, M. De Bastiani, M. Gandini, A. Petrozza, *J. Am. Chem. Soc.* **2014**, *136*, 17730; d) S. D. Stranks, V. M. Burlakov, T. Leijtens, J. M. Ball, A. Goriely, H. J. Snaith, *Phys. Rev. Appl.* **2014**, *2*, 034007.
[27] a) W. J. Yin, T. T. Shi, Y. F. Yan, *Appl. Phys. Lett.* **2014**, *104*, 063903; b) J. Kim, S. H. Lee, J. H. Lee, K. H. Hong, *J. Phys. Chem. Lett.* **2014**, *5*, 1312.
[28] M. Lax, *Phys. Rev.* **1960**, *119*, 1502.
[29] a) J. Lloyd-Hughes, T. I. Jeon, *J. Infrared, Millimeter, Terahertz Waves* **2012**, *33*, 871; b) R. Ulbricht, E. Hendry, J. Shan, T. F. Heinz, M. Bonn, *Rev. Mod. Phys.* **2011**, *83*, 543; c) M. C. Beard, G. M. Turner, C. A. Schmuttenmaer, *Phys. Rev. B* **2000**, *62*, 15764.
[30] P. Langevin, *Ann. Chim. Phys.* **1903**, *28*, 433.
[31] A. Haug, *J. Phys. C: Solid State Phys.* **1983**, *16*, 4159.
[32] A. Amat, E. Mosconi, E. Ronca, C. Quarti, P. Umari, M. K. Nazeeruddin, M. Grätzel, F. De Angelis, *Nano Lett.* **2014**, *14*, 3608.
[33] A. Haug, *J. Phys. C: Solid State Phys.* **1984**, *17*, 6191.
[34] a) W. Lochmann, *Phys. Status Solidi A* **1977**, *40*, 285; b) M. Takeshima, *Phys. Rev. B* **1982**, *25*, 5390; c) M. Takeshima, *Phys. Rev. B* **1981**, *23*, 771.
[35] M. A. Perez-Osorio, M. R. Filip, R. L. Milot, J. Patel, L. M. Herz, M. B. Johnston, F. Giustino, unpublished.
[36] A. Miyata, A. Mitioglu, P. Plochocka, O. Portugall, J. T.-W. Wang, S. D. Stranks, H. J. Snaith, R. J. Nicholas, *Nat. Phys.* **2015**, *11*, 582.
[37] J. M. Frost, K. T. Butler, F. Brivio, C. H. Hendon, M. van Schilfgaarde, A. Walsh, *Nano Lett.* **2014**, *14*, 2584.
[38] M. D. Xiao, F. Z. Huang, W. C. Huang, Y. Dkhissi, Y. Zhu, J. Etheridge, A. Gray-Weale, U. Bach, Y. B. Cheng, L. Spiccia, *Angew. Chem. Int. Ed.* **2014**, *53*, 9898.
[39] C. J. Docherty, P. Parkinson, H. J. Joyce, M. H. Chiu, C. H. Chen, M. Y. Lee, L. J. Li, L. M. Herz, M. B. Johnston, *ACS Nano* **2014**, *8*, 11147.

